Bifurcation study of blood flow control in the kidney

Ashlee N. Ford Versypt[a,1], **Elizabeth Makrides**[b,*,1], **Julia C. Arciero**[c], **Laura Ellwein**[d], and **Anita T. Layton**[e]

[a]School of Chemical Engineering, Oklahoma State University, Stillwater, OK 74078, USA

[b]Division of Applied Mathematics, Brown University, Providence, RI 02912, USA

[c]Department of Mathematical Sciences, Indiana University-Purdue University Indianapolis, Indianapolis, IN 46202, USA

[d]Department of Mathematics and Applied Mathematics, Virginia Commonwealth University, Richmond, VA 23284, USA

[e]Department of Mathematics, Duke University, Durham, NC 27708, USA

Abstract

Renal blood flow is maintained within a narrow window by a set of intrinsic autoregulatory mechanisms. Here, a mathematical model of renal hemodynamics control in the rat kidney is used to understand the interactions between two major renal autoregulatory mechanisms: the myogenic response and tubuloglomerular feedback. A bifurcation analysis of the model equations is performed to assess the effects of the delay and sensitivity of the feedback system and the time constants governing the response of vessel diameter and smooth muscle tone. The results of the bifurcation analysis are verified using numerical simulations of the full nonlinear model. Both the analytical and numerical results predict the generation of limit cycle oscillations under certain physiologically relevant conditions, as observed *in vivo*.

Keywords

Bifurcation analysis; Delay differential equation; Renal hemodynamics; Myogenic response; Tubuloglomerular feedback

1. Introduction

Many biological systems exhibit spontaneous limit cycle oscillations. The mechanisms that give rise to such biological oscillators are intrinsically nonlinear; indeed, no linear system has robust limit cycle behavior. One example of biological limit cycle oscillations occurs in the kidney [1,2]. The kidney regulates the balance of water, salt, and blood pressure via filtration, reabsorption, and secretion of the appropriate amounts of water and solutes across the epithelia of renal tubules known as nephrons. A nephron consists of a glomerulus, which is a bundle of capillaries, and a tubule whose walls consist of a single layer of epithelial

[*]Corresponding author. Tel.: +1 919 593 5992. elizabeth_makrides@brown.edu (E. Makrides).
[1]The first two authors contributed equally.

cells. Blood is delivered via the afferent arteriole to the glomerulus, where the filtration process begins. Blood cells and large plasma proteins are retained in the blood stream, while fluid and smaller solutes (now called filtrate) are forced out into Bowman's capsule, the entrance of the tubule. The resulting filtrate travels through the tubule, where the transformation of the filtrate into urine is initiated. Along the tubule, the filtrate (tubular fluid) composition is altered by transport processes in the epithelial cells of the renal tubule. In particular, the thick ascending limb (TAL), a water-impermeable portion of the tubule in a zone called the loop of Henle, actively and passively transports sodium chloride from tubular fluid into the interstitium outside of the tubule where molecules and ions can be reabsorbed by the bloodstream through nearby capillaries.

To maintain normal renal function, fluid flow through the nephron must be kept within a narrow range. This is accomplished primarily by two physiological regulatory mechanisms: the myogenic response and tubuloglomerular feedback (TGF). The myogenic response induces vasoconstriction in response to increases in blood pressure. In TGF, changes in the chloride ion concentration in the TAL are detected by a collection of epithelial cells at the exit of the TAL called the macula densa (MD). This generates feedback signals that alter the afferent arteriolar smooth muscle tone in order to regulate the glomerular filtration rate. Fig. 1 is a schematic diagram illustrating the anatomy involved in these regulatory mechanisms. The reader may also refer to [3] for additional detail on kidney physiology.

Spontaneous fluctuations of fluid flow and oscillating intratubular pressure have been observed in the rat kidney [1,2,4–8]. Mathematical models of the TGF mechanism have successfully simulated these phenomena [9–12], and sensitivity analysis of these models has suggested the oscillatory or steady state behavior depends on physical and transport characteristics of the TAL. We have recently developed a renal hemodynamics model that combines both the myogenic and TGF mechanisms and used the model to study renal autoregulation [13]. In the present study, we use this model to explore the influence of key bifurcation parameters, including the feedback loop sensitivity, delay, and time constants that govern changes in the diameter and smooth muscle tone of the afferent arteriole. Frequencies of periodic solutions simulated from our model are in agreement with those observed in the literature [14].

We present the details of the first analytical bifurcation analysis on the renal hemodynamics model with both autoregulatory mechanisms. We compare the bifurcation results to the full numerical simulations of the mathematical model for certain parameter values. The bifurcation analysis allows us to understand the global behaviors of the model(i.e., its behaviors over a very large range of parameters), as opposed to direct numerical simulations, which typically cover only a small range of parameters and must be repeated for each combination of parameter values. The major contribution of the present work is the mathematical formulation for the bifurcation analysis that facilitates the exploration of the parameter space in a way that augments the current experimental capabilities for determining the physiological responses in different parameter ranges.

2. Model formulation

The mathematical model used in this study to investigate potential bifurcation parameters was recently described [13]. Briefly, the model captures the flow dynamics along a short loop of Henle in a rat kidney by coupling a partial differential equation (PDE) describing chloride ion transport along the TAL of a short-loop nephron with a system of ordinary differential equations (ODEs) describing vessel wall mechanics of the afferent arteriole. The resulting system includes the effects of both the myogenic and TGF responses. The model takes the form

$$\frac{\partial}{\partial t}C(x,t) = -\left(\frac{1}{\pi r^2}\right)F(D(t))\frac{\partial}{\partial x}C(x,t) - \frac{2}{r}\left(\frac{V_{\max}C(x,t)}{K_m + C(x,t)} + p(C(x,t) - C_e(x))\right), \quad (2.1)$$

$$\frac{d}{dt}D(t) = \frac{1}{t_d}\frac{2}{P_{\text{avg},c}}\left(\frac{P_{\text{avg}}D(t)}{2} - T_{\text{total}}(D(t), A(t))\right), \quad (2.2)$$

$$\frac{d}{dt}A(t) = \frac{1}{t_a}\left(A_{\text{total}}(C(L, t-\tau), D(t)) - A(t)\right), \quad (2.3)$$

where $C(x, t)$ is the concentration of chloride ions in the TAL at position x and time t, with $x = 0$ at the bend in the loop of Henle and $x = L$ at the upper end of the TAL at the MD, while $D(t)$ and $A(t)$ are the diameter and smooth muscle tone (activation), respectively, of the afferent arteriole. The functional forms of $F(D(t))$ and $C_e(x)$ are given in Eqs. (2.4)–(2.6). As given explicitly in Eqs. (2.7)–(2.11), T_{total} is a function of $D(t)$ and $A(t)$, while A_{total} is a function of $D(t)$ and $C(L, t − \tau)$. The parameter τ gives the time required for transmitting the signal of the chloride ion concentration sensed in the MD to the afferent arteriole, including any associated lag in response; thus the system is properly one of delay differential equations (DDEs) with time delay τ. Values for all parameters appearing in Eqs. (2.1)–(2.3), as well as parameters appearing in the subsidiary functions detailed below, are given in Table 1. We refer to these as reference values, and to the resulting model solution as the reference state.

The PDE (2.1) represents axial advective chloride ion transport, outward-directed active solute transport, and transepithelial chloride ion diffusion. The flow rate, $F(D(t))$, appearing in the advective term of Eq. (2.1) has the explicit form

$$F(D(t)) = \alpha\beta Q_A = \alpha\beta\frac{\pi D(t)^4 \Delta P}{128\mu l}. \quad (2.4)$$

Here Q_A is the afferent arteriole flow rate which, in accordance with Poiseuille's law, depends on diameter, $D(t)$; pressure drop along the afferent arteriole, P; viscosity, μ; and afferent arteriole segment length, l. The parameter β represents the fraction of the afferent arteriole flow entering the loop of Henle. The quantity $Q = \beta Q_A$ is commonly referred to as the single nephron glomerular filtration rate (SNGFR), and α is the portion of the SNGFR that is not reabsorbed along the proximal tubule or the descending limb of the loop of Henle

before entering the TAL. Note that the TAL is assumed to be water impermeable, so that fluid flow along the TAL is constant in space, although it may vary in time.

The second term in Eq. (2.1) represents active NaCl reabsorption and is assumed to follow standard Michaelis–Menten kinetics. The last term describes chloride ion diffusion across the TAL with permeability p, while $C_e(x)$ is the extratubular chloride ion concentration, which is assumed to be time independent. $C_e(x)$ is given as [11]

$$C_e(x) = C_0(Be^{-2x/L} + (1 - B)), \quad (2.5)$$

where

$$B = \frac{1 - C_e(L)/C_0}{1 - e^{-2}}. \quad (2.6)$$

The extra- and intratubular chloride ion concentrations are assumed to be equal at the bend of the loop of Henle, so that the boundary condition for chloride ion concentration is given by a constant: $C(0, t) = C_0 = 275$ mM [11].

We use a previously developed vessel wall mechanics model [22,23] to predict changes in the diameter and smooth muscle tone of the afferent arteriole according to the myogenic and TGF mechanisms. The quantities P_{avg} and $P_{\mathrm{avg},c}$ appearing in Eq. (2.2) refer to midpoint pressures in the afferent arteriole; these are determined by the incoming pressure and pressure drop, i.e., $P_{\mathrm{avg}} = P - \Delta P/2$, where P is the intraluminal pressure entering the afferent arteriole. $P_{\mathrm{avg},c}$ is the midpoint pressure with the control (baseline) incoming pressure of 100 mmHg, whereas P_{avg} may vary. In the present study, the pressure P is fixed at 100 mmHg so that P_{avg} does not change and the dynamics over a wide parameter range can be assessed. In our previous work [13], we explored the effects of pressure change on the system by varying afferent arterial pressure between 60 and 180 mmHg. Future studies will combine both investigations to assess simultaneously the effect of varying parameter values and average pressure values on the appearance of limit cycle oscillations.

The total tension in the afferent arteriole wall is expressed as a sum of passive and active components:

$$T_{\mathrm{total}}(D(t), A(t)) = T_{\mathrm{pass}}(D(t)) + A(t)T_{\mathrm{act}}^{\max}(D(t)), \quad (2.7)$$

where T_{pass} describes passive tension as an exponential function of diameter,

$$T_{\mathrm{pass}}(D(t)) = c_{\mathrm{pass}}\exp\left(c_{\mathrm{pass},1}(D(t)/D_0 - 1)\right), \quad (2.8)$$

and $T_{\mathrm{act}}^{\max}$ represents maximally active tension as a Gaussian function of diameter,

$$T_{\mathrm{act}}^{\max}(D(t)) = c_{\mathrm{act}}\exp\left[-\left(\frac{D(t)/D_0 - c_{\mathrm{act},1}}{c_{\mathrm{act},2}}\right)^2\right]. \quad (2.9)$$

Finally, in Eq. (2.3) the level of smooth muscle tone, A_{total}, is modeled as a sigmoidal function of a stimulus, S_{tone}, which includes both the myogenic response and TGF mechanism. Thus,

$$A_{\text{total}}(C(L, t - \tau), D(t)) = \frac{1}{1 + \exp(-S_{\text{tone}}(C(L, t - \tau), D(t)))}, \quad (2.10)$$

where

$$S_{\text{tone}}(C(L, t - \tau), D(t)) = c_{\text{myo}} \frac{P_{\text{avg}} D(t)}{2} + \frac{c_2}{1 + \exp(-c_{\text{TGF}}(C(L, t - \tau) - C_{\text{MD}}))} - c_{\text{tone}}. \quad (2.11)$$

With all parameters set to their reference values as given in Table 1, we refer to the steady state model solution as the reference state, since this is the baseline from which other simulations—which may proceed to limit cycle oscillations or return to the steady state upon perturbation—are run. The reference state values of afferent arteriolar diameter, activation, and flow rate, along with SNGFR and flow rate entering the TAL are given in Table 2. For comparison, we include experimentally observed values for these quantities obtained under normal physiological conditions in rats. The smooth muscle activation of the afferent arteriole, $A(t)$, is a dimensionless variable ranging from 0 to 1, with 0 representing no smooth muscle activation, and 1 maximal smooth muscle activation—see Eq. (2.7). We choose our reference steady state to represent a state of average muscle tone activation, i.e., $A = 0.5$. This choice then dictates the value of the c_{tone} parameter. As in [13], the parameter value for c_2 was optimized in a least squares sense to arteriolar flow values obtained from an empirical feedback relation [12], and $C_{\text{MD}} = 32.32$ mM to be consistent with the expected value of the chloride ion concentration in the macula densa [26]. The reference value of β is set such that $Q = 30.0$ nl/min, which, as noted in Table 2, is a typical value for the SNGFR observed in rats. The reader is also referred to [13] for comparison of model solutions to experimental data over a range of afferent arterial pressures from 60 to 180 mmHg.

3. Analytical and numerical methods

The present study seeks to better understand the dynamic behaviors of the renal autoregulatory system and the stability of steady state solutions. Small, transient perturbations in blood flow may result from an animal's heartbeat, respiration, or motion. After activating the hemodynamics feedback responses, these perturbations may die out, allowing tubular fluid flow to return to a steady state, or the perturbations may grow, evolving into a limit cycle oscillation. The precise outcome depends on the characteristics of the system. Using the model detailed in Section 2, we implement numerical and analytical approaches to predict the asymptotic behavior of the *in vivo* tubular fluid dynamics that occur in response to a perturbation.

In the first approach, the model is solved numerically for various combinations of model parameters. Although this yields a solution to the full nonlinear problem, employing this approach involves characterizing model behavior via an undirected exploration of the full space of physiologically relevant parameter values. Bifurcation analysis provides a second

and complementary approach, directing subsequent numerical simulation to parameter regions that are both dynamically interesting and biologically relevant.

In this section, the algorithms used to solve the model equations numerically and to simulate the effects of perturbations are described, and a characteristic equation is derived and analyzed from a linearization of the model equations. In Section 4, we demonstrate the complementary nature of these two approaches.

3.1. Numerical simulation and perturbation algorithm

To explore the dynamics of the model for specific sets of model parameters, the model solution can be obtained by direct numerical computation. The model equations given by Eqs. (2.1)–(2.3) are coupled and must be solved simultaneously. The chloride ion concentration from Eq. (2.1) is used by Eq. (2.3) with a time delay, τ. The diameter D from Eq. (2.2) is used to update the inlet flow rate $F(D(t))$ for Eq. (2.1). This system of equations is solved numerically by first using the method of lines [27] and the upwind differencing scheme to reduce the PDE in Eq. (2.1) to a system of ODEs in time and then using the MATLAB solver DDE23 [28] to solve the resulting system of DDEs with constant delay τ. A uniformly-spaced grid of 161 points is used to discretize the PDE unless otherwise indicated, and the maximum time-step size in the DDE23 solver is set to 0.1 s to prevent high frequency numerical oscillations that may result from steps that are too large.

To simulate the dynamic effect of a perturbation, a small step perturbation in flow rate is held for a moderate duration, and then flow rate is allowed to vary with changes in D and A induced by the chloride ion concentration deviation from steady state that resulted from the perturbation in flow rate. The simulation algorithm for this numerical experiment involves four steps. First, the reference state is initialized by determining the steady state values of D and activation A with the reference state parameters specified, and by computing the steady state spatial distribution of chloride ions $C(x)$ with constant inlet flow rate F calculated by the steady state value of D. Second, the solver DDE23 is used to solve the coupled model equations numerically as described above with the reference state conditions given as a constant history vector for the solver. This part of the simulation algorithm determines the coupled steady state solution at the reference state. Third, a 1% step increase in the flow rate is imposed for 15.7 s, which is the time interval required for fluid to move through the entire TAL at the reference state F. These values for the small pulse magnitude and duration match those used in the analogous bifurcation study for TGF-associated oscillations [11]. While F is perturbed by this constant step change, D and A are held constant, and the PDE for chloride ion transport with a constant flow rate is solved numerically by the solver DDE23 with the function for the system of DDEs modified to maintain constant D, A, and F for the perturbation interval. Thus, $C(x)$ continues to change during this flow perturbation interval. In the final step of the numerical experiment, F, D, and A are reinitialized to their reference state values and then are allowed to change in response to the perturbed $C(x)$, which is specified as the dynamic history vector by means of the numerical solution from the perturbation time interval. The solver DDE23 is used to solve the model equations until a steady state or limit cycle oscillation develops after the perturbation interval (total

simulation time of at least 1000 s) to determine the dynamics of the DDE system in response to a perturbation from the steady state.

Spectral plots shown in Section 4 are computed using the discrete Fourier transform routine FFT in MATLAB. Time profiles for D are computed as described in this section, with sampling frequency 10 Hz and total length 1000 s or 10,000 points, and are then trimmed to remove the steady state portion of the profile prior to the pulse. The steady state value of D is subtracted from the time-varying value at each point of the remaining time series in order to remove the zero-frequency signal. The number of points in the discrete Fourier transform is set to 16,384, the smallest power of two greater than 10,000.

3.2. Bifurcation analysis

While numerical simulations can be run for a variety of model parameter values, bifurcation analysis is used to quickly identify system behavior for a larger parameter space.

3.2.1. General form of the characteristic equation—To begin, we derive a general form for the characteristic equation that allows for straightforward substitutions or model refinements in the future. The model equations (2.1)–(2.3) can be written in the following general form:

$$\frac{\partial}{\partial t}C(x,t)=F^{(0)}(D(t);\mu_0)\frac{\partial}{\partial x}C(x,t)+F^{(1)}(C(x,t);\mu_1) \quad (3.1)$$

$$\frac{d}{dt}D(t)=F^{(2)}(D(t),A(t);\mu_2) \quad (3.2)$$

$$\frac{d}{dt}A(t)=F^{(3)}(D(t),A(t),C(L,t-\tau);\mu_3), \quad (3.3)$$

where the particular forms of the functions $F^{(i)}$ and the vectors of parameters μ_i, $i = 0,\ldots, 3$, are determined by Eqs. (2.1)–(2.11).

Linearizing about a steady state solution $(C(\bar{x}), \bar{D}, \bar{\ })$ yields

$$\frac{\partial}{\partial t}\begin{pmatrix} C(x,t) \\ D(t) \\ A(t) \end{pmatrix} = \begin{pmatrix} F^{(0)}(\overline{D})\frac{\partial}{\partial x}+F^{(1)}_C(\overline{C}(x)) & F^{(0)}_D(\overline{D})\overline{C}'(x) & 0 \\ 0 & F^{(2)}_D(\overline{D},\overline{A}) & F^{(2)}_A(\overline{D},\overline{A}) \\ F^{(3)}_C(\overline{D},\overline{A},\overline{C}(L))\mathscr{L} & F^{(3)}_D(\overline{D},\overline{A},\overline{C}(L)) & F^{(3)}_A(\overline{D},\overline{A},\overline{C}(L)) \end{pmatrix} \times \begin{pmatrix} C(x,t) \\ D(t) \\ A(t) \end{pmatrix} \quad (3.4)$$

where $(C(x, t), D(t), A(t))^T$ is properly a solution on $[t − \tau, t]$, and we define $\mathscr{L}C(x, t) \coloneqq C(L, t − \tau)$. Differentiation with respect to x is denoted by $'$ throughout, while $F^{(i)}_A$ indicates the partial derivative with where respect to A, with the analogous convention for C and D. The dependence on parameters μ_i is suppressed.

Making the ansatz

$$\begin{pmatrix} C(x,t) \\ D(t) \\ A(t) \end{pmatrix} = \begin{pmatrix} f(x) \\ b_1 \\ b_2 \end{pmatrix} e^{\lambda t} \quad (3.5)$$

gives

$$\lambda \begin{pmatrix} f(x) \\ b_1 \\ b_2 \end{pmatrix} = \begin{pmatrix} F^{(0)}(\overline{D})f'(x) + F_C^{(1)}(\overline{C}(x))f(x) + F_D^{(0)}(\overline{D})\overline{C}'(x)b_1 \\ F_D^{(2)}(\overline{D},\bar{A})b_1 + F_A^{(2)}(\overline{D},\bar{A})b_2 \\ F_C^{(3)}(\overline{D},\bar{A},\overline{C}(L))f(L)e^{-\lambda\tau} + F_D^{(3)}(\overline{D},\bar{A},\overline{C}(L))b_1 + F_A^{(3)}(\overline{D},\bar{A},\overline{C}(L))b_2 \end{pmatrix},$$

which can be rewritten as

$$\begin{pmatrix} F^{(0)}(\overline{D})f'(x) \\ 0 \\ 0 \end{pmatrix}$$
$$= \begin{pmatrix} \lambda - F_C^{(1)}(\overline{C}(x)) & -F_D^{(0)}(\overline{D})\overline{C}'(x) & 0 \\ 0 & \lambda - F_D^{(2)}(\overline{D},\bar{A}) & -F_A^{(2)}(\overline{D},\bar{A}) \\ 0 & -F_D^{(3)}(\overline{D},\bar{A},\overline{C}(L)) & \lambda - F_A^{(3)}(\overline{D},\bar{A},\overline{C}(L)) \end{pmatrix}$$
$$\times \begin{pmatrix} f(x) \\ b_1 \\ b_2 \end{pmatrix}$$
$$- \begin{pmatrix} 0 \\ 0 \\ F_C^{(3)}(\overline{D},\bar{A},\overline{C}(L))f(L)e^{-\lambda\tau} \end{pmatrix} \quad (3.6)$$

so that the first row of Eq. (3.6) is an ODE. Solving for b_2 in terms of b_1, λ, and $f(L)$ from the third row of Eq. (3.6) gives

$$b_2 = \frac{F_D^{(3)}(\overline{D},\bar{A},\overline{C}(L))b_1 + F_C^{(3)}(\overline{D},\bar{A},\overline{C}(L))f(L)e^{-\lambda\tau}}{\lambda - F_A^{(3)}(\overline{D},\bar{A},\overline{C}(L))}.$$

Substituting this solution for b_2 into the second row of Eq. (3.6) gives an expression for b_1:

$$b_1 = \frac{-F_A^{(2)}(\overline{D},\bar{A})F_C^{(3)}(\overline{D},\bar{A},\overline{C}(L))f(L)e^{-\lambda\tau}}{(\lambda - F_D^{(2)}(\overline{D},\bar{A}))(F_A^{(3)}(\overline{D},\bar{A},\overline{C}(L)) - \lambda) + F_A^{(2)}(\overline{D},\bar{A})F_D^{(3)}(\overline{D},\bar{A},\overline{C}(L))}. \quad (3.7)$$

The following differential equation results from the first row:

$$f'(x) = \left(\frac{\lambda - F_C^{(1)}(\overline{C}(x))}{F^{(0)}(\overline{D})} \right) f(x) - \left(\frac{F_D^{(0)}(\overline{D})\overline{C}'(x)}{F^{(0)}(\overline{D})} \right) b_1, \quad (3.8)$$

where b_1 is given in Eq. (3.7). Enforcing the boundary condition $f(0) = 0$, which is equivalent to assuming that $C(0, t)$ is fixed at $\overline{C}(0)$, gives the solution

$$f(x) = -\left(\frac{F_D^{(0)}(\overline{D})}{F^{(0)}(\overline{D})}\right) b_1 \exp\left(-\int_0^x \left(\frac{F_C^{(1)}(\overline{C}(y)) - \lambda}{F^{(0)}(\overline{D})}\right) dy\right) \times \int_0^x \overline{C}'(z) \exp\left(\int_0^z \left(\frac{F_C^{(1)}(\overline{C}(y)) - \lambda}{F^{(0)}(\overline{D})}\right) dy\right) dz. \quad (3.9)$$

Evaluating at $x = L$, rearranging, and canceling the $f(L)$ that appears in b_1 gives the following characteristic equation:

$$1 = K\int_0^L \overline{C}'(z) e^{\lambda(L-z)/F^{(0)}(\overline{D})} \exp\left(-\int_z^L \left(\frac{F_C^{(1)}(\overline{C}(y))}{F^{(0)}(\overline{D})}\right) dy\right) dz, \quad (3.10)$$

where

$$K = e^{-\lambda\tau}\left(\frac{F_D^{(0)}}{F^{(0)}}\right)\left(\frac{F_A^{(2)} F_C^{(3)}}{(\lambda - F_D^{(2)})(F_A^{(3)} - \lambda) + F_A^{(2)} F_D^{(3)}}\right) \quad (3.11)$$

and each $F^{(i)}$ is evaluated at the appropriate steady state.

3.2.2. Model-specific characteristic equation—Using the general form of the characteristic equation from Eqs. (3.10) and (3.11), the particular form of the characteristic equation can be defined for the model equations given by Eqs. (2.1)–(2.3). First substituting these model equations into Eqs. (3.1)–(3.3) gives the following $F^{(i)}$:

$$F^{(0)}(D(t)) = -\frac{\alpha\beta D(t)^4 \Delta P}{128 r^2 l\mu}, \quad (3.12)$$

$$F^{(1)}(C(x,t)) = -\frac{2}{r}\left(\frac{V_{\max} C(x,t)}{K_M + C(x,t)} + p(C(x,t) - C_e(x))\right), \quad (3.13)$$

$$F^{(2)}(D(t), A(t)) = \frac{1}{t_d}\frac{2}{P_{\mathrm{avg},c}}\left(\frac{P_{\mathrm{avg}} D(t)}{2} - (T_{\mathrm{pass}}(D(t)) + A(t) T_{\mathrm{act}}^{\max}(D(t)))\right), \quad (3.14)$$

and

$$F^{(3)}(D(t), A(t), C(L, t-\tau)) = \frac{1}{t_a}\left(\frac{1}{1 + \exp(-S_{\mathrm{tone}}(C(L, t-\tau), D(t)))} - A(t)\right). \quad (3.15)$$

Using the particular form of $F^{(1)}$, we can further simplify the characteristic equation (3.10) to eliminate the steady state derivative $\overline{C}'(x)$ in the integral. Recalling Eq. (3.1), $\overline{C}(x)$ must satisfy

$$\overline{C}'(x) = -\frac{1}{F^{(0)}(D)} F^{(1)}(\overline{C}(x)) = \frac{2}{F^{(0)}(D)r}(V(\overline{C}(x)) + p(\overline{C}(x) - C_e(x))), \quad (3.16)$$

where $V(C(x,t)) = \dfrac{V_{\max}C(x,t)}{K_M + C(x,t)}$. Differentiating again with respect to x and rearranging, we find

$$-F^{(0)}(\overline{D})\frac{\overline{C}''(x)}{\overline{C}'(x)} - \frac{2}{r}\frac{pC_e'(x)}{\overline{C}'(x)} = -\frac{2}{r}\left(V_C(\overline{C}(x)) + p\right) \quad (3.17)$$

with the terms arranged so that the right-hand side is $F_C^{(1)}(\overline{C}(x))$. Substituting into Eq. (3.10) gives

$$
\begin{aligned}
1 &= K\int_0^L \overline{C}'(z)e^{\lambda(L-z)/F^{(0)}(\overline{D})}\ \exp\ \left(\int_z^L \left(\frac{\overline{C}''(y)}{\overline{C}'(y)} + \frac{2pC_e'(y)}{r\overline{C}'(y)F^{(0)}(\overline{D})}\right)dy\right)dz\\
&= K\int_0^L \overline{C}'(z)e^{\lambda(L-z)/F^{(0)}(\overline{D})}\ \exp\ \left(\ln\left(\frac{\overline{C}'(L)}{\overline{C}'(z)}\right)\right.\\
&\quad + \left.\int_z^L \left(\frac{2pC_e'(y)}{r\overline{C}'(y)F^{(0)}(\overline{D})}\right)dy\right)dz\\
&= \overline{C}'(L)K\int_0^L e^{\lambda(L-z)/F^{(0)}(\overline{D})}\ \exp\ \left(\int_z^L \left(\frac{2pC_e'(y)}{r\overline{C}'(y)F^{(0)}(\overline{D})}\right)dy\right)dz.
\end{aligned}
\quad (3.18)
$$

By analogy with earlier works [11,29], we define the sensitivity γ by

$$\gamma = \frac{\overline{C}'(L)F_D^{(0)}F_A^{(2)}F_C^{(3)}}{F^{(0)}} = \frac{\overline{C}'(L)F_D^{(0)}(\overline{D})F_A^{(2)}(\overline{D},\bar{A},\overline{C}(L))F_C^{(3)}(\overline{D},\bar{A},\overline{C}(L))}{F^{(0)}(\overline{D})}. \quad (3.19)$$

Substituting Eq. (3.19) into Eq. (3.18) yields an alternate form for the characteristic equation:

$$1 = \frac{\gamma e^{-\lambda\tau}}{(\lambda - F_D^{(2)})(F_A^{(3)} - \lambda) + F_A^{(2)}F_D^{(3)}}\int_0^L e^{\lambda(L-z)/F^{(0)}(\overline{D})}\times\exp\ \left(\int_z^L \left(\frac{2pC_e'(y)}{r\overline{C}'(y)F^{(0)}(\overline{D})}\right)dy\right)dz. \quad (3.20)$$

In earlier models involving only the TAL, a measure called the sensitivity was defined as a product of the derivative of the chloride concentration profile with respect to position evaluated at the MD, and the derivative of the flow with respect to the chloride concentration evaluated at the reference state [11]. Here, the first term in the numerator of Eq. (3.19) corresponds to the first term in the earlier definition, while the last three terms in the numerator correspond to the second term, i.e., the derivative of the flow. The sensitivity, also referred to as the gain, quantifies the effect of changes in input on output variables.

3.2.3. Evaluation of characteristic equation—To compute two-parameter bifurcation diagrams, solutions of the characteristic equation (3.18) satisfying $\rho := \mathrm{Re}\,\lambda = 0$ are determined via gradient descent. All parameters other than the specified bifurcation parameters are fixed at reference values given in Section 2 unless otherwise indicated, with $\omega := \mathrm{Im}\,\lambda$ and one of the two bifurcation parameters allowed to vary. Contours for particular

values of ω are found by fixing ω at the indicated value while allowing ρ to vary. The steady state concentration profile $\bar{C}(x)$ used in these computations is obtained by direct numerical computation as described in Section 3.1. Derivatives appearing in Eq. (3.18) are computed by a midpoint approximation and integrals are computed using a trapezoidal rule.

4. Model results

From the bifurcation analysis in Section 3.2, a two-parameter bifurcation diagram for sensitivity, γ, and time delay, τ, is created by solving the characteristic equation (3.18) and setting ρ := Re λ = 0. As shown in Fig. 2, a transition from a stable steady state to limit cycle oscillations is predicted when either τ is increased while γ is held constant or when γ is increased for a fixed τ. Direct numerical experiments are conducted as described in Section 3.1 to simulate the change in system dynamics when τ is increased from 1 s (point (I) in Fig. 2) to τ = 2 s (point (II) in Fig. 2). All other parameters are set to their reference values so that sensitivity remains at its reference state value (γ = 4.754). As seen explicitly in the bottom two panels of Fig. 2, the numerical simulations confirm the stable steady state and limit cycle oscillations in the parameter regions predicted by the bifurcation analysis.

Additional simulations varying the initial chloride concentration C_0 to within ±10% and ±50% of its original value (results not shown) demonstrate good agreement with the dynamics predicted in Fig. 2. While Fig. 2 strictly applies to a linearization about the reference steady state, the results are an accurate guide to dynamic behavior for initial conditions at an extreme distance from those used in our study.

By virtue of the transcendental characteristic equation (3.18), numerous additional bifurcation curves for which ρ = 0 exist beyond the initial supercritical Hopf bifurcation indicated in Fig. 2. Fig. 3 shows a subset of these curves, along with their corresponding frequencies ω := Im λ. Curves corresponding to the same frequencies occur in sets that are roughly repeated with increasing τ. Moreover, the frequencies increase for each set of curves with increasing values of γ. Although the frequency varies along each curve, considering the frequency near the minimum of each and taking ω = 0.3 as a base frequency, we see that the first set of curves above the Hopf bifurcation corresponds to a frequency of about twice the base, the second set to a frequency close to three times the base, and the third to a frequency around four times the base. These results may be compared with earlier work on a related simplified model [11, see in particular Fig. 4], as well as [9]. Here several of the curves are connected, which is a feature that was not present or noted in earlier works. Note that, in order to capture the mathematically interesting behavior of these curves, the results are shown for larger values of both γ and τ than we expect to be physiologically relevant.

The information in Fig. 3 indicates that a parameter region exists in which limit cycle oscillations of twice the fundamental frequency should occur. Point (III) in Fig. 3 lies inside this region, and Fig. 4 shows time series profiles for diameter and the associated power spectra for points (II) and (III). As in Fig. 2, point (II) corresponds to reference state conditions but with τ = 2 s. Point (III) corresponds to reference state conditions except τ = 0.1 s and the parameter cTGF is set to 6.33×10^5 so that γ = 10.0. The power spectra in Fig. 4 demonstrate that point (III) parameter values yield limit cycle oscillations that display a

first harmonic dominant frequency, i.e., double that of the underlying fundamental frequency. Multiple frequencies are observed immediately following the perturbation, with oscillations at the fundamental frequency decaying as the first harmonic oscillations grow, so that the corresponding two peaks are of comparable intensity for the first 100 s after perturbation (data not shown). The observed frequencies for both points (II) and (III) agree with the predictions from the bifurcation analysis, as indicated by the values of ω in Fig. 3. Moreover, the values predicted by the model align with experiments conducted by Basar and Weiss in isolated rat kidneys [14], in which power density peaks were observed at frequencies between 40–70 mHz and 90–120 mHz. The lower frequencies are also consistent with experiments conducted by Leyssac and colleagues [1,6]. Since the time constants t_a and t_d also affect the frequency of oscillations (as shown in more detail in the following), the model supports a wide range of dominant oscillatory frequencies, from less than 30 mHz (e.g., for large τ) to over 100 mHz.

In addition to the two-dimensional bifurcation diagram for γ and τ (Figs. 2 and 3), the relationships between additional bifurcation parameters can be explored. Fig. 5a shows the bifurcation diagram for the time constant for diameter, t_d, versus τ, with fixed time constant for activation, t_a, while Fig. 5b shows the bifurcation diagram for t_a and τ with fixed t_d. Both diagrams indicate that increasing τ past a threshold curve results in limit cycle oscillations. In each diagram, the solid blue curve indicates the stability threshold for the reference value of the fixed time constant. There is a qualitative difference between the blue bifurcation curves: the curve for t_d versus τ intersects the *y*-axis, whereas the curve for t_a versus τ has upward curvature and does not extend to the *y*-axis. However, the shape of each bifurcation curve depends on the non-varying time constant, rather than reflecting a fundamental difference between t_d and t_a. This is demonstrated by the dashed red curves, which indicate the stability threshold with particular non-reference values of the fixed time constant chosen to illustrate the opposite behavior with respect to intersection with the *y*-axis. We observe that $t_a = 1$ s is a smaller than would be expected under experimental conditions; it is employed here to demonstrate that the qualitative difference in the blue bifurcation curves depends on other parameter values and is not dictated by the model equations. As seen in Figs. 6 and 7, stability may be restored by increasing either t_a or t_d substantially; however, the parameter values at which stability is reestablished are outside the physiologically relevant range.

The intersection of the bifurcation curves with the *y*-axis observed for certain parameter choices in Fig. 5 indicates that limit cycle oscillations may exist even when τ is 0. Exploring this further in the bifurcation diagram for t_a versus t_d with fixed τ = 0 s (Fig. 6), the limit cycle oscillations are enclosed within a region of parameter space, while a stable steady state exists outside this region. Fig. 6b indicates the frequencies associated with the limit cycle oscillations by depicting contours for ω. The portions of the ω contours outside the region of limit cycle oscillations correspond to the characteristic frequencies of damped oscillations that occur as the system returns to steady state after perturbation. The highest frequency oscillations, in excess of 50 mHz, are found for values of t_a and t_d below 20 s.

As τ is increased from 0 to 3 s, the region corresponding to limit cycle oscillations expands steadily (Fig. 7), but no additional bifurcation curves appear. Both Figs. 6 and 7 include a

much larger parameter range than is physiologically relevant in order to capture the full extent of the regions of limit cycle oscillations. Fig. 7b rescales Fig. 7a at finer resolution to highlight the physiologically relevant region where the bifurcation curves are difficult to distinguish on the larger scale. The physiological ranges for τ_d and τ_a follow from values used in [23]. For $\tau = 2$ s, the stable region is disconnected, and for $\tau = 3$ s the stable region is confined to a very small area near the origin.

5. Discussion

We have analyzed the dynamics of a mathematical model of blood flow control in the kidney using parameter values consistent with rat physiology. The model assumes that renal blood flow is controlled by two major autoregulatory mechanisms: the myogenic response, by which increases in blood pressure induce vasoconstriction, and the tubuloglomerular feedback (TGF), through which the glomerular filtration rate is regulated based on changes in the luminal chloride ion concentration at the macula densa. This model is used to identify a variety of dynamic behaviors that can arise for parameters within physiological and pathophysiological parameter regimes. These behaviors, which include limit-cycle oscillations, were identified and characterized by analyzing the characteristic equation that arises from a linearization of the model equations and were further explored by direct numerical simulation of the solutions for the full model equations. We note that nested periodic solutions were not observed. TGF-mediated oscillations have been observed in a number of experimental studies [4–8]. To the best of our knowledge, this is the first study that performs a bifurcation analysis on a renal hemodynamics model that includes both TGF and myogenic responses.

Prior to this work, many mathematical models with varying degrees of complexity have been used to analyze kidney autoregulation considering only the TGF mechanism [9,11,29–35]. Glomerular filtration rate is also regulated by the myogenic response, which, together with TGF, acts upon the smooth muscle cells of the afferent arteriole and induces vasoconstriction or vasodilation. By sharing a common effector, the two mechanisms are expected to interact. Thus, the bifurcation analysis and numerical simulations presented in this study enable a fuller understanding of the interactions between the myogenic response and TGF mechanism and the resulting dynamics.

Our results indicate that the time constants associated with the afferent arteriole muscle mechanics (t_d and t_a) are important bifurcation parameters in addition to the delay and sensitivity, which were previously studied in models involving only the TGF mechanism. By simultaneously varying the time delay, τ, and the time constants t_a and t_d, we indicate how these three parameters interact to shift the border between a stable steady state and limit cycle oscillations. Increasing the response time of the afferent arteriole initially lowers the stability of the autoregulatory system before reestablishing stability at much longer response times (Figs. 6 and 7). In a previous vessel wall mechanics model that includes the effects of the myogenic response, the ratio of t_d to t_a was found to determine stability [36]. Here, the values of t_d and t_a are found to be important individually, as can be seen by considering any ray from the origin in Figs. 6 and 7. In fact, the time constants t_a and t_d interact to produce a closed region in two-dimensional parameter space in which limit cycle oscillations are

observed. The results presented here further demonstrate the importance of these parameters in determining oscillatory frequency and indicate that the combined model supports a wide range of dominant frequencies. The oscillatory frequencies predicted by our bifurcation analysis and observed in numerical simulations of model solutions are consistent with those detected experimentally [1,6,14].

A few renal hemodynamics models represent both TGF and myogenic mechanisms. In separate studies, Marsh et al. [37,38] and Sgouralis and Layton [39] formulated comprehensive models of renal autoregulation that represented the dynamic interactions of TGF and myogenic mechanisms. These models included a detailed representation of the afferent arteriole that captured both intracellular calcium dynamics and membrane potential. In contrast, the present study adopts a simpler representation of the arteriolar response to regulatory signals. The simplicity of our arteriolar model enables an analytical bifurcation analysis, which provides a more comprehensive understanding of the correspondence between different parameter regimes and solution behavior.

Certain simplifying assumptions in the present model may impact the validity of the dynamic behaviors predicted for different parameter regimes. First, the TAL is represented as a rigid tubule with uniform radius and transport parameters. Results from a previous modeling study representing the TAL as a tubule with compliant walls suggest that tubular compliance may significantly reduce the stability of the TGF system [30]. Another study [32] suggests that inhomogeneities in tubular radius or in maximum chloride transport rate, as indicated in experimental measurements [40,41], further increase the tendency of the system to oscillate. Second, the bifurcation parameters may also undergo substantial changes as exemplified by spontaneously hypertensive rats, which appear to exhibit higher TGF gain [42–44], compared to normotensive rats. Together with stronger internephron coupling, in which the TGF signal of one nephron is partially transmitted to a neighboring nephron sharing the same cortical radial artery, tubular spontaneously hypertensive rats exhibit irregular TGF-mediated oscillations that appear to have characteristics consistent with deterministic chaos [6,45]. This observation can be explained, in part, by the bifurcation results of our model, which suggest that at higher TGF gain, the stability of the system is significantly reduced. Third, the present model considers a single afferent arteriole and loop of Henle in isolation. It is, however, important to note that TGF in each nephron does not operate independently of other nephrons. Indeed, the TGF systems of nephrons whose afferent arterioles arise from a common interlobular artery are known to be coupled [46], with the TGF signal propagating rapidly via the afferent arteriolar endothelium. Previous studies of dynamics of nephrons coupled via their TGF system indicate that internephron coupling increases the likelihood of TGF-mediated oscillations. Combining several copies of the present model, which incorporates both TGF and the myogenic response, may shed new light on the importance of internephron coupling on the dynamic behavior of the system. The stability of the resulting system can be investigated via the bifurcation analysis used in the present study, following the approach of [31,47].

Acknowledgments

References

1. Leyssac P, Baumbach L. An oscillating intratubular pressure response to alterations in Henle loop flow in the rat kidney. Acta Physiol. Scand. 1983; 117:415–419. [PubMed: 6880803]

2. Leyssac P. Further studies on oscillating tubulo-glomerular feedback responses in the rat kidney. Acta Physiol. Scand. 1986; 126:271–277. [PubMed: 3705986]

3. Eaton, D.; Pooler, J. Vander's Renal Physiology. 8th. New York: McGraw-Hill Medical; 2013.

4. Cupples W, Novak P, Novak V, Salevsky F. Spontaneous blood pressure fluctuations and renal blood flow dynamics. Am. J. Physiol. Renal Physiol. 1996; 270:F82–F89.

5. Cupples W. Angiotensin II conditions the slow component of autoregulation of renal blood flow. Am. J. Physiol. Renal Physiol. 1993; 264:F515–F522.

6. Holstein-Rathlou N, Leyssac P. TGF-mediated oscillations in the proximal intratubular pressure: differences between spontaneously hypertensive rats and Wistar-Kyoto rats. Acta Physiol. Scand. 1986; 126:333–339. [PubMed: 3962682]

7. Holstein-Rathlou N, Leyssac P. Differences in tubuloglomerular feedback—oscillatory activity between spontaneously hypertensive and Wistar-Kyoto rats. J. Hypertens. 1985; 3:S343–S345.

8. Yip K, Holstein-Rathlou N, Marsh D. Mechanisms of temporal variation in single-nephron blood flow in rats. Am. J. Physiol. Renal Physiol. 1993; 264:F427–F434.

9. Layton AT, Moore LC, Layton HE. Multistability in tubuloglomerular feedback and spectral complexity in spontaneously hypertensive rats. Am. J. Physiol. Renal Physiol. 2006; 291:F79–F97. [PubMed: 16204416]

10. Budu-Grajdeanu P, Moore L, Layton H. Effect of tubular inhomogeneities on filter properties of thick ascending limb of Henle's loop. Math. Biosci. 2007; 209(2):564–592. [PubMed: 17499314]

11. Layton HE, Pitman EB, Moore LC. Bifurcation analysis of TGF-mediated oscillations in SNGFR. Am. J. Physiol. Renal Physiol. 1991; 261:F904–F919.

12. Layton HE, Pitman EB, Moore LC. Instantaneous and steady-state gains in the tubuloglomerular feedback system. Am. J. Physiol. Renal Physiol. 1995; 268:F163–F174.

13. Arciero JC, Ellwein L, Ford Versypt AN, Makrides E, Layton AT. Modeling blood flow control in the kidney. Proc. IMA. 2014 in press.

14. Basar E, Weiss C. Time series analysis of spontaneous fluctuations of the flow in the perfused rat kidney. Pflügers Arch. 1970; 319:205–214. [PubMed: 5529093]

15. Pfaller, W. Structure Function Correlation on Rat Kidney: Quantitative Correlation of Structure and Function in the Normal and Injured Rat Kidney. New York: Springer-Verlag; 1982.

16. Johnson, P. Handbook of Physiology. The Cardiovascular System. Vascular Smooth Muscle. Bethesda, MD: Am. Physiol. Soc; 1981. The myogenic response; p. 409-442.

17. Loutzenhiser R, Bidani A, Chilton L. Renal myogenic response: kinetic attributes and physiologic role. Circ. Res. 2002; 90:1316–1324. [PubMed: 12089070]

18. Myers BD, Deen WM, Brenner BM. Effects of norepinephrine and angiotensin ii on the determinants of glomerular ultrafiltration and proximal tubule fluid reabsorption in the rat. Circ. Res. 1975; 37:101–110. [PubMed: 1149180]

19. Moore L, Schnermann J, Yarimizu S. Feedback mediation of SNGFR autoregulation in hydropenic and DOCA- and salt-loaded rats. Am. J. Physiol. Renal Physiol. 1979; 237:F63–F74.

20. Pries AR, Secomb TW, Gessner T, Sperandio MB, Gross JF, Gaehtgens P. Resistance to blood flow in microvessels *in vivo*. Circ. Res. 1994; 75:904–915. [PubMed: 7923637]

21. Casellas D, Dupont M, Bouriquet N, Moore L, Artuso A, Mimran A. Anatomic pairing of afferent arterioles and renin cell distribution in rat kidneys. Am. J. Physiol. Renal Physiol. 1994; 267:F931–F936.

22. Carlson BE, Arciero JC, Secomb TW. Theoretical model of blood flow autoregulation: roles of myogenic, shear-dependent, and metabolic responses. Am. J. Physiol. Heart Circ. Physiol. 2008; 295:H1572–H1579. [PubMed: 18723769]

23. Arciero J, Carlson B, Secomb T. Theoretical model of metabolic blood flow autoregulation: roles of ATP release by red blood cells and conducted responses. Am. J. Physiol. Heart Circ. Physiol. 2008; 295:H1562–H1571. [PubMed: 18689501]

24. Treek B, Roald AB, Tenstad O, Aukland K. Effect of exogenous and endogenous angiotensin ii on intrarenal distribution of glomerular filtration rate in rats. Kidney Int. 2002; 541:1049–1057.

25. de Rouffignac C, Monnens L. Functional and morphologic maturation of superficial and juxtamedullary nephrons in the rat. J. Physiol. 1969; 48:119–129.

26. Schnermann, J.; Briggs, J. Function of the juxtaglomerular apparatus: control of glomerular hemodynamics and renin secretion. In: Alpern, RJ.; Hebert, SC., editors. Seldin and Giebisch's the Kidney: Physiology and Pathophysiology. 4th. Amsterdam, Boston: Elsevier Academic Press; 2008. p. 589-626.

27. Schiesser, WE. The Numerical Method of Lines: Integration of Partial Differential Equations. San Diego: Academic Press; 1991.

28. Shampine L, Thompson S. Solving DDEs in MATLAB. Appl. Numer. Math. 2001; 37:441–458.

29. Holstein-Rathlou NH, Marsh DJ. A dynamic model of the tubuloglomerular feedback mechanism. Am. J. Physiol. Renal Fluid Electrolyte Physiol. 1990; 258:F1448–F1459.

30. Layton A. Feedback-mediated dynamics in a model of a compliant thick ascending limb. Math. Biosci. 2010; 228:185–194. [PubMed: 20934438]

31. Layton A, Moore L, Layton H. Multistable dynamics mediated by tubuloglomerular feedback in a model of coupled nephrons. Bull. Math. Biol. 2009; 71:515–555. [PubMed: 19205808]

32. Ryu H, Layton A. Effect of tubular inhomogeneities on feedback-mediated dynamics of a model of a thick ascending limb. Math. Med. Biol. 2012; 30:191–212. [PubMed: 22511507]

33. Ryu H, Layton A. Tubular fluid flow and distal NaCl delivery mediated by tubuloglomerular feedback in the rat kidney. J. Math. Biol. 2014; 68(4):1023–1049. [PubMed: 23529284]

34. Hattaway, A. Ph.D. thesis. University of Massachusetts Amherst; 2004. Modelling tubuloglomerular feedback in coupled nephrons.

35. Holstein-Rathlou N. A closed-loop analysis of the tubuloglomerular feedback mechanism. Am. J. Physiol. Renal Physiol. 1991; 261:F880–F889.

36. Arciero J, Secomb T. Spontaneous oscillations in a model for active control of microvessel diameters. Math. Med. Biol. 2012; 29:163–180. [PubMed: 21525236]

37. Marsh D, Sosnovtseva O, Chon K, Holstein-Rathlou N. Nonlinear interactions in renal blood flow regulation. Am. J. Physiol. Regul. Integr. Comp. Physiol. 2005; 288:R1143–R1159. [PubMed: 15677526]

38. Marsh D, Sosnovtseva O, Pavlov A, Yip K, Rathlou NH. Frequency encoding in renal blood flow regulation. Am. J. Physiol. Regul. Integr. Comp. Physiol. 2005; 288:R1160–R1167. [PubMed: 15661968]

39. Sgouralis I, Layton A. Theoretical assessment of renal autoregulatory mechanisms. Am. J. Physiol. Renal Physiol. 2014; 306:F1357–F1371. [PubMed: 24623150]

40. Garg L, Mackie S, Tischer C. Effects of low potassium diet on Na–K–ATPase in rat nephron segments. Pflügers Arch. 1982; 394:113–117. [PubMed: 6289258]

41. Knepper M, Danielson R, Saidel G, Post R. Quantitative analysis of renal medullary anatomy in rats and rabbits. Kidney Int. 1977; 12:313–323. [PubMed: 604620]

42. Brännström K, Morsing P, Arendshorst W. Exaggerated tubuloglomerular feedback activity in genetic hypertension is mediated by ANG II and AT_1 receptors. Am. J. Physiol. Renal Physiol. 1996; 270:F749–F755.

43. Leyssac P, Holstein-Rathlou N. Tubulo-glomerular feedback response: enhancement in adult spontaneously hypertensive rats and effects of anaesthetics. Pflügers Arch. 1989; 413:267–272. [PubMed: 2717373]

44. Takabatake T, Ushiogi Y, Ohta K, Hattori N. Attenuation of enhanced tubuloglomerular feedback activity in SHR by renal denervation. Am. J. Physiol. Renal Physiol. 1990; 258:F980–F985.

45. Yip K, Holstein-Rathlou N, Marsh D. Chaos in blood flow control in genetic and renovascular hypertensive rats. Am. J. Physiol. Renal Physiol. 1991; 261:F400–F408.

46. Holstein-Rathlou N. Synchronization of proximal intratubular pressure oscillations: evidence for interaction between nephrons. Pflügers Arch. 1987; 408:438–443. [PubMed: 3601634]

47. Layton A, Bowen M, Wen A, Layton H. Feedback-mediated dynamics in a model of coupled nephrons with compliant thick ascending limbs. Math. Biosci. 2011; 230:115–127. [PubMed: 21329704]
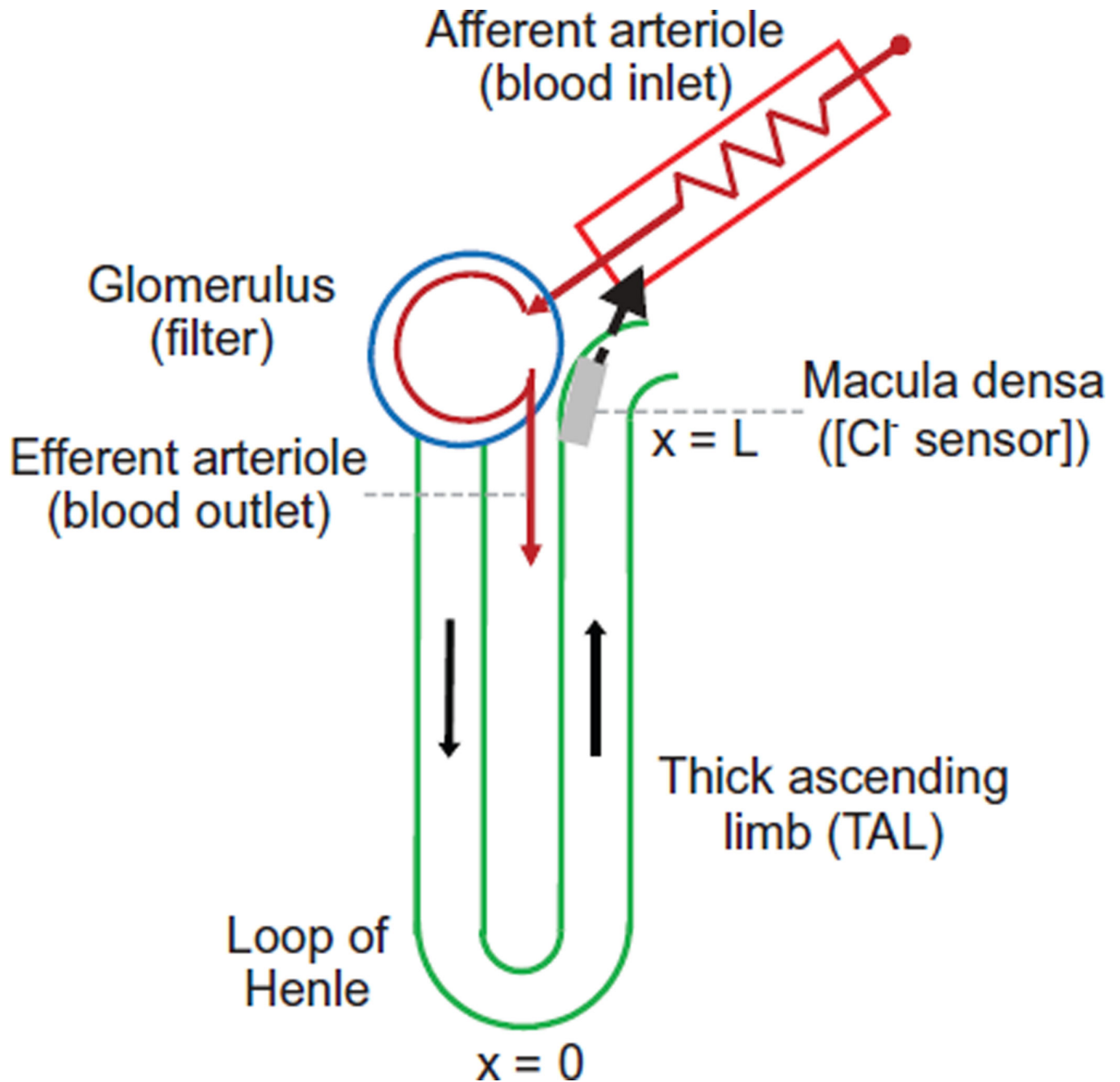
Fig. 1.
Schematic diagram of the major components of a kidney nephron. As detailed in Section 2, the present model includes a partial differential equation (PDE) for the chloride ion concentration in the thick ascending limb (TAL), and ordinary differential equations (ODEs) for the afferent arteriolar diameter and smooth muscle tone. The chloride concentration at the end of the TAL is sensed by the macula densa (MD), causing adjustments in the afferent arteriolar diameter and tone, which in turn impact the chloride ion concentration by changing the flow rate entering the TAL.
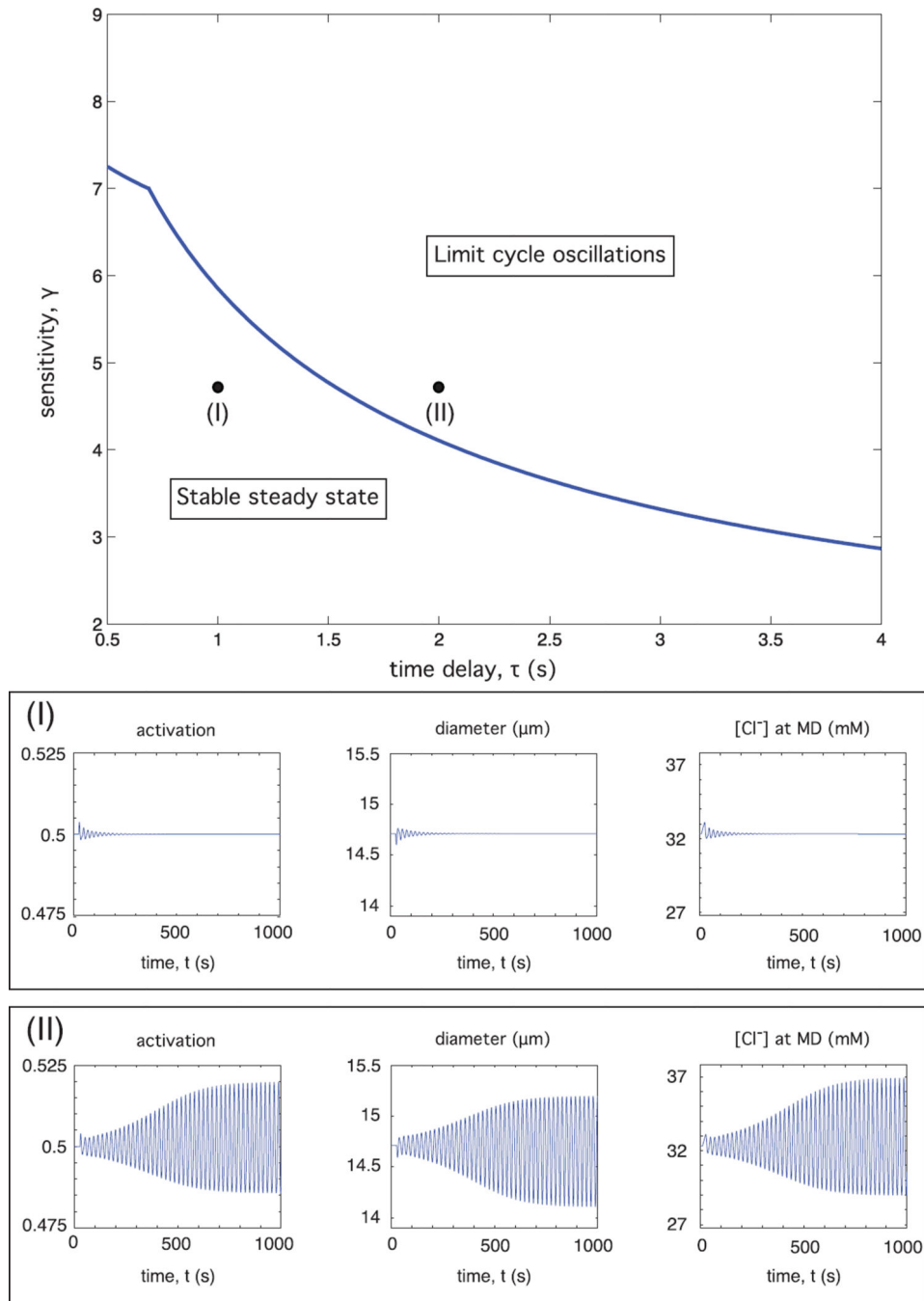
Fig. 2.
Upper panel: sensitivity, γ, as given by Eq. (3.19) plotted against time delay, τ. The curve indicates the transition from a stable steady state (lower left) to limit cycle oscillations (upper right). Points (I) and (II) indicated in the upper panel lie on either side of the predicted bifurcation from a stable steady state to limit cycle oscillations. Lower two panels: dynamic profiles for afferent arteriolar smooth muscle activation, $A(t)$; afferent arteriolar diameter, $D(t)$; and chloride ion concentration at the MD, $C(L, t)$, after transient perturbation

from steady state. The profiles in the middle panel correspond to point (I) with $\tau = 1$ s, while the profiles in the bottom panel correspond to the point (II) with $\tau = 2$ s.
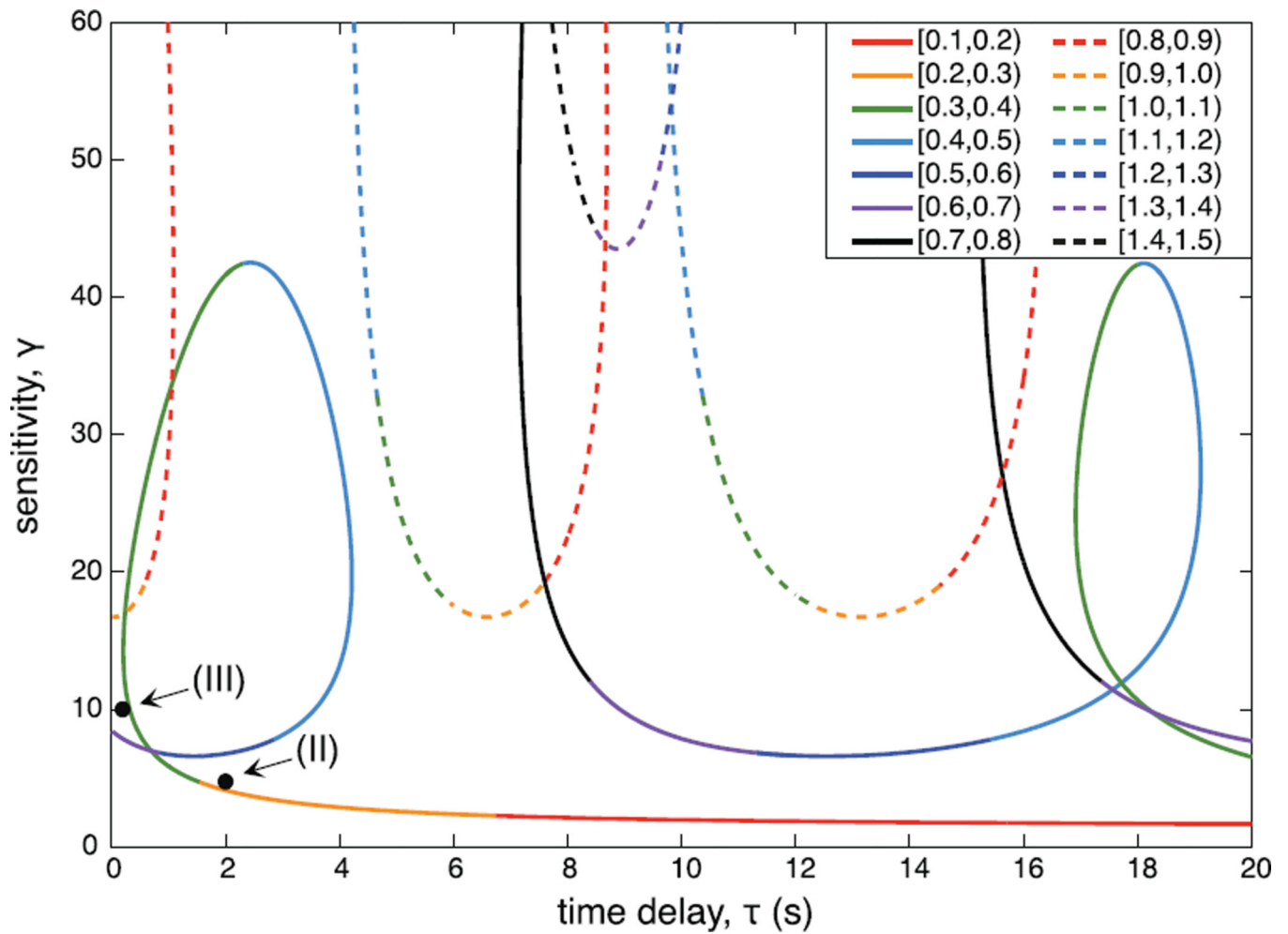
Fig. 3.
Sensitivity, γ, plotted against time delay, τ. Each curve corresponds to a solution of the characteristic equation (3.18) with $\rho = 0$, and ω in the range indicated by the line color and style. The points labeled (II) and (III) have (τ, γ) coordinates (2.0, 4.75) and (0.1, 10.0) respectively, with the former corresponding to point (II) in Fig. 2. Power spectra for the oscillatory solutions associated with these parameter values are displayed in Fig. 4. (For interpretation of the references to color in this figure legend, the reader is referred to the web version of this article.)
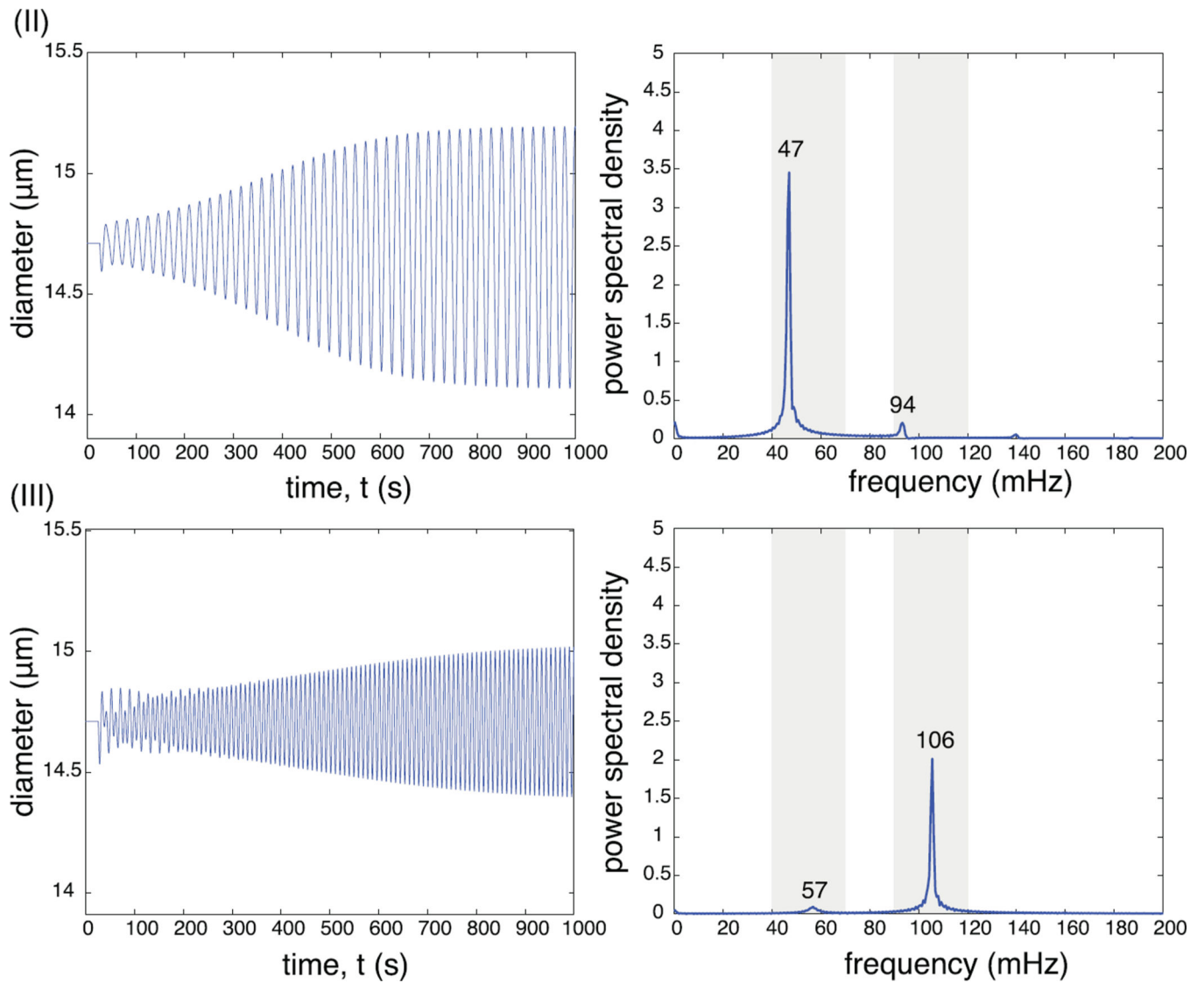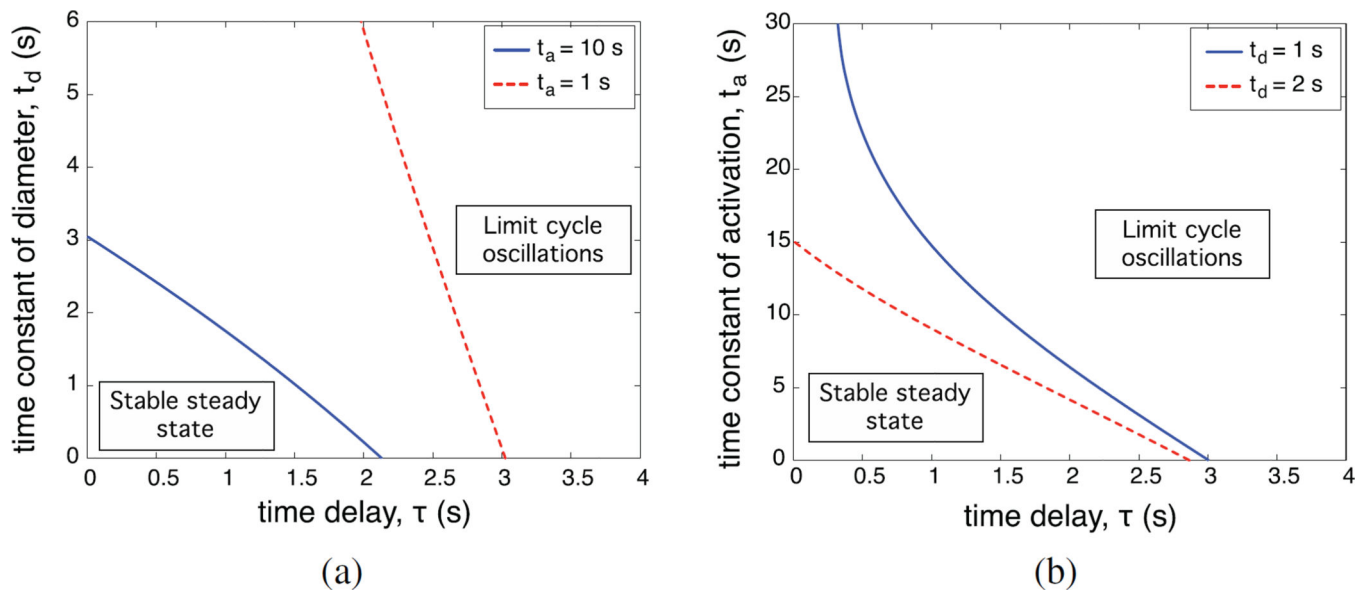
Fig. 4.
Time profiles for diameter (left) with associated power spectra (right). The upper and lower panels correspond to the points labeled (II) and (III), respectively, in Fig. 3. The upper left plot is repeated from Fig. 2 for comparison. Shaded regions indicate experimentally observed frequencies [14].

Fig. 5.
Bifurcation curves for time constants (t_d for diameter and t_a for activation) plotted against time delay, τ: (a) varying t_d with fixed values of t_a and (b) varying t_a with fixed values of t_d. Solid blue curves correspond to the reference values of the fixed time constant, and dashed red curves to non-reference values. Each curve indicates the location of the transition from a stable steady state (below and to the left of the curve) to limit cycle oscillations (above and to the right of the curve). Thus the region between the curves in (a) corresponds to a stable steady state when $t_a = 1$ s and to limit cycle oscillations when $t_a = 10$ s. In (b), the region between the curves corresponds to a stable steady state when $t_d = 1$ s and to limit cycle oscillations when $t_d = 2$ s. (For interpretation of the references to colour in this figure legend, the reader is referred to the web version of this article.)
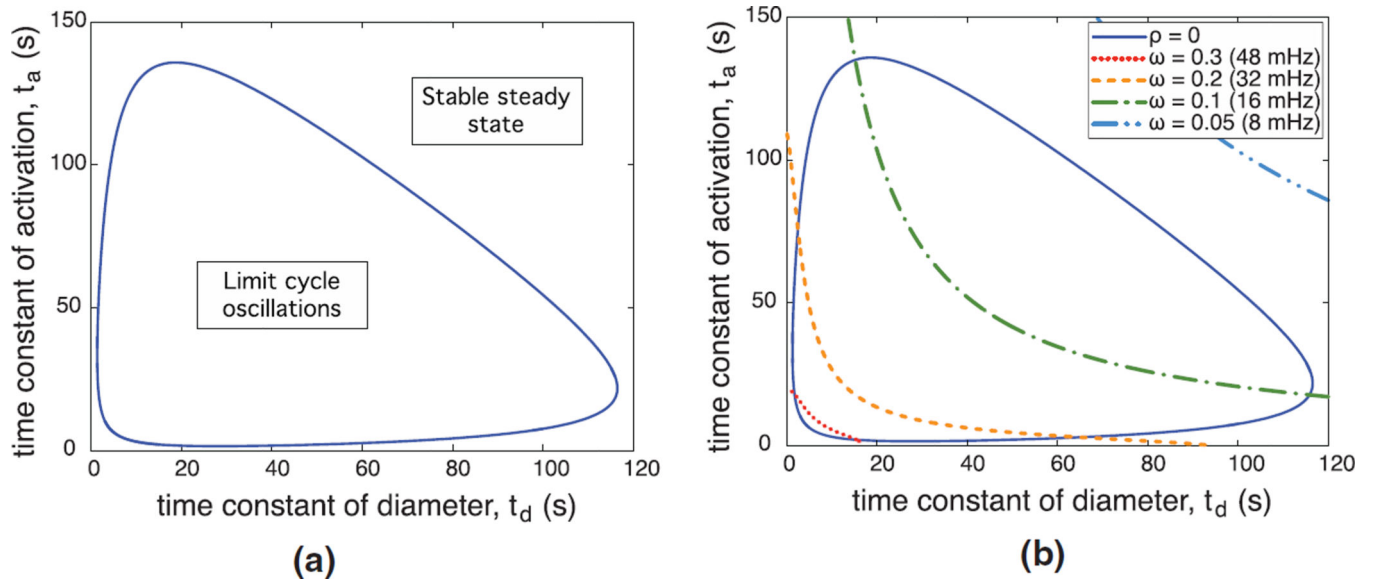
Fig. 6.
Time constant for activation, t_a, plotted against the time constant for diameter, t_d, with fixed time delay, $\tau = 0$ s. (a) The curve corresponds to $\rho = 0$, indicating the transition from a stable steady state to limit cycle oscillations. (b) The solid dark blue curve is repeated from (a), while the remaining colored curves with varying line styles indicate contours of the frequency ω. (For interpretation of the references to colour in this figure legend, the reader is referred to the web version of this article.)
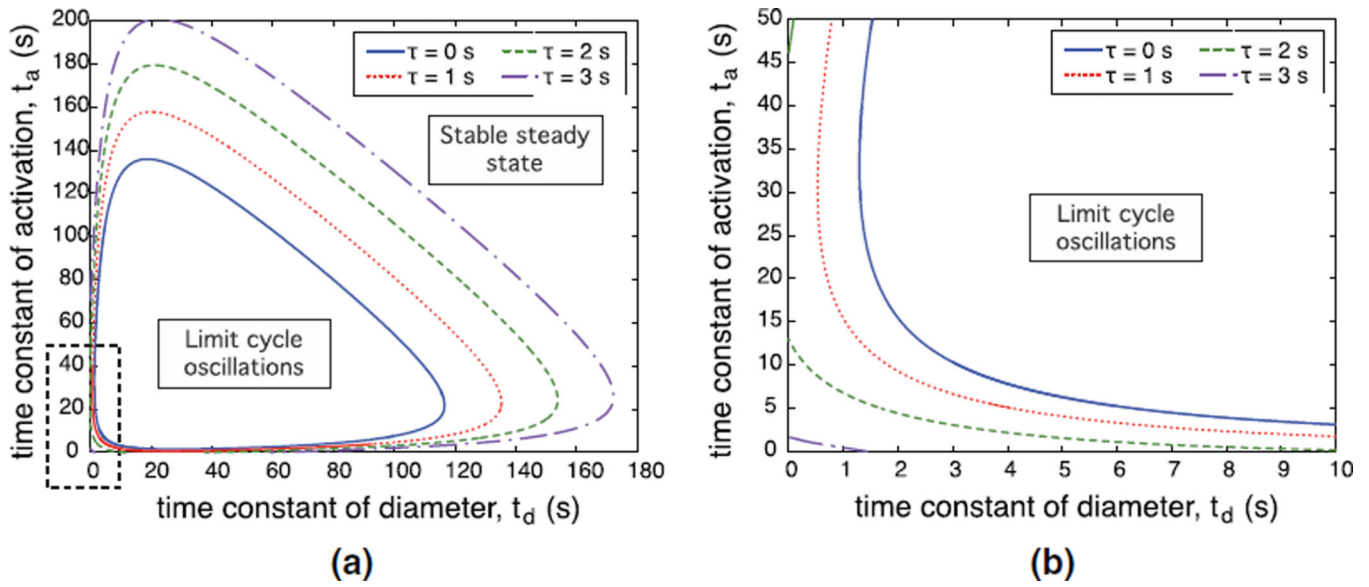
Fig. 7.
Time constant for activation, t_a, plotted against the time constant for diameter, t_d, with fixed values of time delay, τ. The dashed box in (a) outlines the physiologically relevant parameter range that is shown at higher magnification in (b).

Table 1

Reference values for all parameters appearing in Eqs. (2.1)–(2.11).

Symbol	Description	Units	Value	Source
r	TAL luminal radius	cm	10.0×10^{-4}	[11]
V_{max}	Maximum active transport rate	mol/cm^{2}s	14.5×10^{-9}	[11]
K_m	Michaelis constant	mM	70.0	[11]
p	TAL Cl$^-$ permeability	cm/s	1.5×10^{-5}	[11]
L	Length of TAL	cm	0.5	[15]
C_0	Luminal [Cl$^-$] at loop of Henle	mM	275.0	[11]
$C_e(L)$	Interstitial [Cl$^-$] at MD	mM	150.0	[11]
t_d	Time constant for AA diameter response	s	1.0	[16, 17]
$P_{avg,c}$	Midpoint pressure in AA, control state	mmHg	75	[18]
P_{avg}	Midpoint pressure in AA, specified	mmHg	75	[18]
t_a	Time constant for activation response	s	10.0	[16, 17]
τ	Time delay, MD to AA response	s	4.0	[11]
β	Glomerular filtration fraction	–	0.084	Calculated
α	Fraction of glomerular filtrate entering TAL	–	0.2	[19]
P	Pressure drop along AA	mmHg	50	[18]
μ	Blood viscosity in AA	cP	4.14	[20]
l	Afferent arteriole segment length	cm	0.031	[21]
c_{pass}	Passive tension strength	dyn/cm	220	[22]
$c_{pass,1}$	Passive tension sensitivity	–	11.47	[22]
D_0	Passive reference AA diameter	μm	33	Calculated
c_{act}	Maximally active VSM peak tension	dyn/cm	274.19	[22]
$c_{act,1}$	Maximally active VSM length dependence	–	0.75	[22]
$c_{act,2}$	Maximally active VSM tension range	–	0.38	[22]
c_{myo}	VSM activation tension sensitivity	cm/dyn	0.159	[11]
c_2	VSM TGF sensitivity	cm/dyn	1.8	Estimated
c_{TGF}	VSM activation [Cl$^-$] sensitivity	cm/dyn	3×10^5	[11]
C_{MD}	[Cl$^-$] at MD	mM	32.32	Calculated
c_{tone}	VSM constant	–	12.59	Estimated

Abbreviations: thick ascending limb (TAL); macula densa (MD); afferent arteriole (AA); vascular smooth muscle (VSM).

Table 2

Model and experimental values for key physiological quantities.

Symbol	Description	Units	Model	Experiment	Reference
D	AA diameter	μm	14.7	14.8 ± 1.0	[17]
A	AA activation	–	0.5	NA	NA
Q_A	AA flow rate	nl/min	355.4	316 ± 24	[24]
Q	SNGFR	nl/min	30.0	36.8 ± 9.1, 28.2 ± 2.1	[25],[24]
F	Flow rate entering TAL	nl/min	6.0	6.9 ± 0.7	[19]

Model steady state values correspond to the solution calculated using parameter values given in Table 1. We refer to the model solution calculated with parameter values from Table 1 as the reference state. Note that the activation, A, is a dimension less variable ranging from 0 to 1. Experimental values are as given in the indicated reference.